

## Large-scale assembly of colloidal nanoparticles and fabrication of periodic subwavelength structures

This article has been downloaded from IOPscience. Please scroll down to see the full text article.

2008 Nanotechnology 19 475604

(<http://iopscience.iop.org/0957-4484/19/47/475604>)

[The Table of Contents](#) and [more related content](#) is available

Download details:

IP Address: 131.252.177.251

The article was downloaded on 03/11/2008 at 20:27

Please note that [terms and conditions apply](#).

# Large-scale assembly of colloidal nanoparticles and fabrication of periodic subwavelength structures

Wei-Lun Min<sup>1</sup>, Peng Jiang<sup>1,3</sup> and Bin Jiang<sup>2</sup>

<sup>1</sup> Department of Chemical Engineering, University of Florida, Gainesville, FL 32611, USA

<sup>2</sup> Department of Mathematics and Statistics, Portland State University, Portland, OR 97201, USA

E-mail: [pjiang@che.ufl.edu](mailto:pjiang@che.ufl.edu).

Received 16 September 2008, in final form 28 September 2008

Published 30 October 2008

Online at [stacks.iop.org/Nano/19/475604](http://stacks.iop.org/Nano/19/475604)

## Abstract

This paper reports a simple and scalable spin-coating technique for assembling 70 nm silica nanoparticles into non-close-packed colloidal crystals over a large area. The thickness of the shear-aligned colloidal crystals can be controlled from hundreds of layers to a single monolayer by adjusting the spin-coating conditions. We further demonstrate that the spin-coated colloidal monolayers can be used as structural templates to pattern sub-100 nm pillar arrays directly on silicon substrates. The resulting subwavelength-structured pillar arrays exhibit excellent broadband antireflective and superhydrophobic properties, which are promising for developing self-cleaning antireflection coatings for crystalline silicon solar cells. This bottom-up approach enables large-scale production of periodic nanostructures with resolution beyond the optical diffraction limit that have important technological applications ranging from high-density data storage and optoelectronics to biological sensing and subwavelength optics.

(Some figures in this article are in colour only in the electronic version)

## 1. Introduction

Large-scale fabrication of sub-100 nm periodic nanostructures is of great interest for the development of new materials with potential applications in areas such as high-density data storage [1, 2], biosensing and bioseparation [3–6], and optoelectronics [7, 8]. A prominent example is the creation of subwavelength-structured moth-eye antireflection coatings (ARCs) for developing high-performance solar cells and optoelectronic devices [9, 10]. These coatings are inspired by the nanostructured corneas of moths which consist of non-close-packed arrays of conical nipples [11]. As the periodicity of the nipple array is small compared to the wavelength of visible light, a graded transition of refractive index between air and cornea is established. This results in superior broadband antireflection performance than traditional single-layer or multilayer dielectric coatings [12–15]. To generate broadband ARCs for optics working in the deep-ultraviolet spectral range for developing next-generation optical projection lithography,

sub-100 nm periodic nipple arrays need to be fabricated in a scalable manner [9]. Unfortunately, current top-down nanolithographic technologies, such as electron-beam lithography, focused ion beam, and interference lithography, suffer from low throughput and high cost, are time consuming, and are only suitable for small areas. In this paper, we report a scalable and inexpensive bottom-up approach for assembling 70 nm diameter silica nanoparticles over large areas and fabricating sub-100 nm periodic nanostructures for developing self-cleaning, broadband moth-eye ARCs for crystalline silicon solar cells.

Self-assembled monolayer or multilayer colloidal crystals have been widely utilized as sacrificial masks to pattern periodic microstructures and nanostructures for a large variety of applications ranging from biosensors and high-density magnetic storage to field-emission displays and miniaturized plasmonic devices [16–25]. However, most of the current colloidal self-assembly techniques suffer from low throughput and incompatibility with standard microfabrication, impeding mass production and on-chip

<sup>3</sup> Author to whom any correspondence should be addressed.

integration of practical devices. It usually takes hours to days to create a centimeter-sized colloidal crystal template by current assemblies [26, 27]. In addition, conventional colloidal templating technology employs submicrometer- to micrometer-scale colloidal particles. Though sub-100 nm features can be fabricated [17], the number density of the templated nanostructures is limited by the relatively large separation between the neighboring particles. Moreover, only close-packed colloidal crystals are available through traditional self-assembly, whereas non-close-packed crystals are preferred for many applications, such as in creating moth-eye ARCs with non-close-packed structures [11].

To resolve the scalability issue of current colloidal assemblies, we have recently developed a versatile spin-coating technique that enables wafer-scale assembly of submicrometer-sized particles (usually 300 nm in diameter) into unusual non-close-packed structures [28, 29]. The technique also provides a scalable templating fabrication platform for producing a large variety of microstructured materials with submicrometer-scale periodicity, such as polymer microvial arrays, two-dimensional (2D) magnetic dots, and metal hole arrays [30–32]. Although this templating platform has significant cost benefit over traditional top-down techniques, many of the templated microstructures can be fabricated by optical lithography, such as interference lithography [33]. To greatly extend the capability of the spin-coating technique in creating periodic nanostructures with resolution beyond the optical diffraction limit, here we demonstrate the scalable production of periodic sub-100 nm features with more than one order of magnitude higher number density than our previous approaches. We also show that both multilayer and monolayer non-close-packed colloidal crystals consisting of 70 nm diameter silica particles can be assembled by shear-induced ordering, and the rheological response during the shear-alignment process is investigated.

## 2. Experimental details

### 2.1. Materials and substrates

All solvents and chemicals, except for tetraethoxysilane (TEOS), were of reagent quality and were used without further purification. TEOS was freshly distilled before use. Ethanol (200-proof) was purchased from Pharmaco Products. Ethoxylated trimethylolpropane triacrylate monomer (ETPTA, SR 454) was obtained from Sartomer. The photoinitiator, Darocur 1173 (2-hydroxy-2-methyl-1-phenyl-1-propanone), was provided by Ciba-Geigy. The silicon wafer primer, 3-acryloxypropyl trichlorosilane (APTCS), was purchased from Gelest. Silicon wafers (2 inch, test grade, n-type, (100)) were obtained from University Wafer. The silicon wafers were primed by swabbing APTCS on the wafer surfaces using cleanroom Q-tips, rinsed with 200-proof ethanol twice, and then baked on a hot plate at 110°C for 2 min. A single-crystalline silicon solar cell with vacuum-deposited silicon nitride antireflection coating was obtained from Plastecs (Webster, MA).

### 2.2. Instrumentation

Scanning electron microscopy was carried out on a JEOL 6335F FEG-SEM. Transmission electron microscopy was performed on a JEOL 2010F TEM. A standard spin coater (WS-400B-6NPP-Lite spin processor, Laurell) was used to spin-coat colloidal suspensions. The polymerization of ETPTA monomer was carried out on a pulsed UV curing system (RC 742, Xenon). Both oxygen and chlorine reactive-ion etching (RIE) were carried out on a Unaxis Shuttlelock RIE/ICP reactive-ion etcher. A Woollam EC 110 ellipsometer was used to measure the nanocomposite thickness. The zeta potential of silica nanoparticles are measured by a Brookhaven ZetaPlus (Brookhaven Instrument Corporation). An ARES LS-1 rheometer was used to characterize the rheological properties of the colloidal suspensions under shear. An HR4000 UV–vis spectrometer and an NIR-512 spectrometer (both from Ocean Optics) were used to measure the specular reflectance from 400 to 1100 nm. The apparent water contact angle was measured using a goniometer (NRL CA goniometer, Ramé-Hart Inc.) with autopipetting and imaging systems.

### 2.3. Preparation of colloidal suspensions

The synthesis of uniform silica nanoparticles with ~70 nm diameter was performed according to [34]. In a typical synthesis, a microemulsion was prepared by rapidly stirring 750 ml of cyclohexane, 30 ml of *n*-hexanol, 95 ml of Triton N-101 surfactant, 35 ml of water, and 8.5 ml of 29.3% aqueous ammonia. 50 ml of freshly distilled TEOS was rapidly added to the above microemulsion and the final solution was stirred at ambient temperature for 2 days. The as-made silica nanoparticles were purified in 200-proof ethanol by multiple (at least six times) centrifugation–ultrasonication cycles to remove the surfactant and unreacted silane. After complete centrifugation of the calculated amount of purified silica dispersion and discarding of the supernatant solvent, the silica colloids were re-dispersed in ETPTA monomer using a Thermodyne Maxi solution mixer. 1% (weight) Darocur 1173 was added as the photoinitiator. The final particle volume fraction was controlled to be ~20%. After filtration through a 5  $\mu$ m syringe filter to remove any large aggregate, the transparent colloidal suspension was stored in an open vial overnight to allow residual ethanol to evaporate.

### 2.4. Spin-coating of colloidal suspensions and photopolymerization

The colloidal suspension was dispersed on a silicon wafer which had been freshly primed by APTCS. The wafer was tilted and rotated to spread the solution to achieve full wafer coverage. The recipe for spin-coating a monolayer of silica nanoparticles was 200 rpm for 1 min, 300 rpm for 1 min, 1000 rpm for 30 s, 3000 rpm for 10 s, 6000 rpm for 10 s, 8000 rpm for 10 s, and 10000 rpm for 26 min. For preparing multilayer colloidal crystals, the spin-coating conditions were the same, except for a shorter spin time in the last step at 10000 rpm. The monomer was then photopolymerized for 4 s using a pulsed UV curing system.

### 2.5. Specular reflection measurements

An HR4000 high-resolution fiber optic UV–vis spectrometer and an NIR-512 spectrometer (both from Ocean Optics) with reflection probes were used for reflectance measurements. A calibrated halogen light source was used to illuminate the sample. The beam spot size was about 3 mm on the sample surface. Measurements were performed at normal incidence and the cone angle of collection was less than 5°. The absolute reflectivity was obtained as the ratio of the sample spectrum to the reference spectrum. The reference spectrum was the optical density obtained from an aluminum-sputtered (1000 nm thickness) silicon wafer. The final value of absolute reflectivity was the average of several measurements obtained from different spots on the sample surface. The resulting reflectivity was calibrated using an Ocean Optics STAN-SSL low-reflectivity specular reflectance standard for templated pillar arrays and an STAN-SSH high-reflectivity specular reflectance standard for flat silicon wafers.

## 3. Results and discussion

The well-established microemulsion method was used to synthesize monodispersed silica nanoparticles with  $\sim 70$  nm diameter [34, 35]. Figure 1 shows a typical transmission electron microscope (TEM) image of the as-made nanoparticles. The diameter of the spheres was determined to be  $72 \pm 6$  nm by averaging over 100 particles using the image analysis software Scion Image. The nanoparticles were purified in 200-proof ethanol by multiple centrifugation–ultrasonication cycles and then dispersed in non-volatile ethoxylated trimethylolpropane triacrylate (ETPTA, SR 454, Sartomer) monomers to make a final particle volume fraction of  $\sim 20\%$  [28]. 1% (by weight) Darocur 1173 (Ciba-Geigy) was added as the photoinitiator. The suspension was disposed on a 3-acryloxypropyl trichlorosilane-primed silicon wafer. The wafer was gradually accelerated to 10 000 rpm and kept at this speed for various durations, using a standard spin coater (WS-400B-6NPP-Lite spin processor, Laurell). The gradual increase of the spin speed was crucial for obtaining uniform coatings over large area; otherwise, patchy samples resulted. The monomer was rapidly polymerized by exposure to ultraviolet radiation using a pulsed UV curing system (RC 742, Xenon) to form ordered colloidal crystal–polymer nanocomposites. More details of the spin-coating process can be found in section 2. Contrary to the distinctive six-arm Bragg diffraction formed on spin-coated crystals consisting of submicrometer-sized particles [28], the resulting nanocomposites were transparent and colorless due to the index match between the silica nanoparticles and the polymer matrix, as well as negligible scattering and diffraction of visible light by subwavelength nanoparticle arrays.

The polymer matrix could be selectively removed by a brief oxygen plasma etch operating at 3 mTorr pressure, 20 SCCM oxygen flow rate, and 50 W for 3 min to release the embedded silica colloidal crystals. Figure 2(A) shows a top-view scanning electron microscope (SEM) image of a multilayer crystal prepared by spin-coating at 10 000 rpm for 10 min. The long-range hexagonal ordering of silica

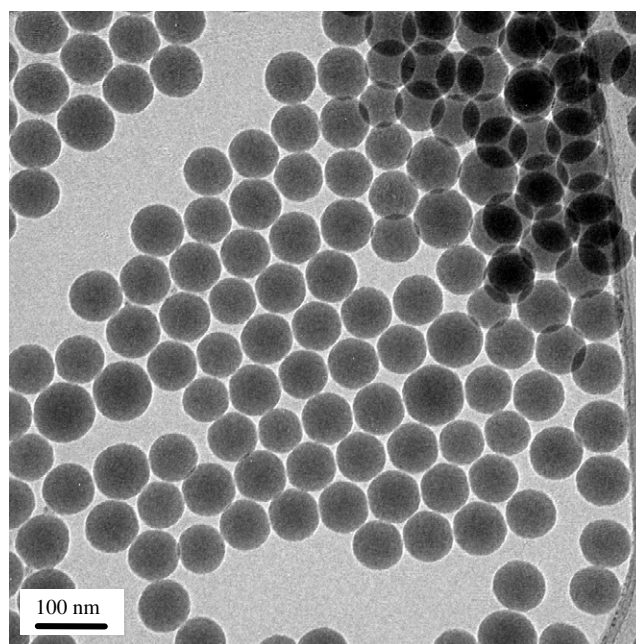


**Figure 1.** TEM image of silica nanoparticles synthesized by the microemulsion method.

nanoparticles is clearly evident from the SEM image and its fast-Fourier transform (inset of figure 2(A)). The magnified SEM image in figure 2(B) shows that the spin-coated colloidal crystal is non-close-packed and that the spheres of the top layer fill in the triangularly arranged crevices made by the non-touching spheres of the second layer. Underneath, hexagonally packed layers throughout the film thickness exhibit similar intralayer non-close-packed structures and good registry between neighboring layers. One of the great advantages of the current spin-coating technique is that the thickness of the spin-coated colloidal crystals can be easily controlled by adjusting the spin speed and duration. Ellipsometry measurements showed that uniform films with thickness ranging from a single monolayer to hundreds of layers could be created over a 2 inch diameter wafer. Figure 2(C) shows an SEM image of a monolayer non-close-packed colloidal crystal consisting of 70 nm particles prepared by spin-coating at 10 000 rpm for 26 min.

The interparticle distance of the non-close-packed colloidal crystal is determined to be  $1.41D$ , where  $D$  is the diameter of the silica spheres, by the first peak of the pair correlation function (PCF; see figure 2(D)),  $g(r)$ , which is calculated from a lower-magnification image as in figure 2(C) as

$$g(r) = \frac{1}{\langle \rho \rangle} \frac{dn(r, r + dr)}{da(r, r + dr)}$$

where  $\langle \rho \rangle$  is the average particle number density and  $r$  is the particle radius. To calculate the PCF, Scion Image software was utilized to extract the particle coordinates. Figure 2(D) shows that the positions of the oscillating PCF peaks agree well with those obtained from a perfect hexagonal lattice with  $\sqrt{2}D$  interparticle distance. This distance is the same as that of spin-coated crystals made of submicrometer-sized particles,

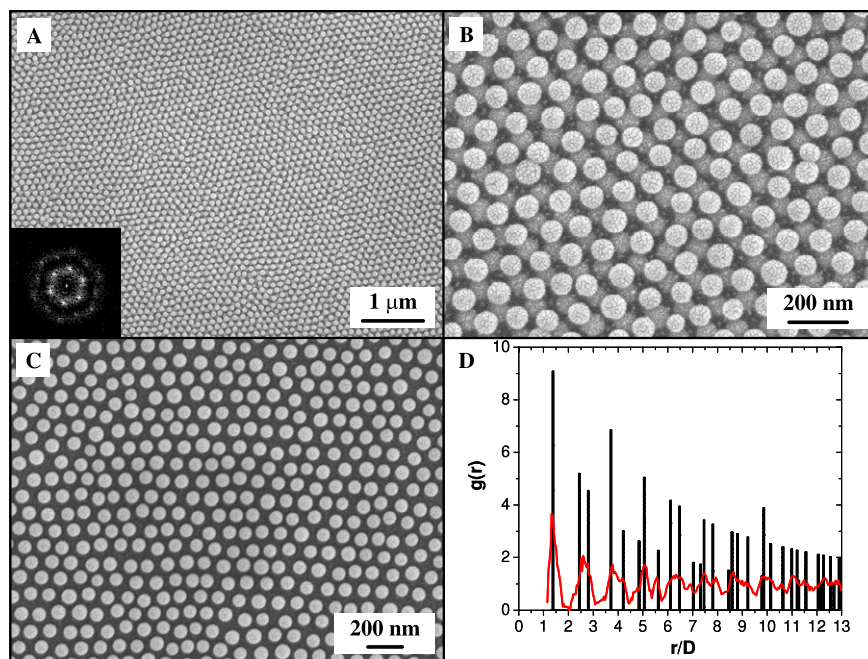


**Figure 2.** (A) SEM image of a multilayer colloidal crystal prepared by spin-coating. The inset showing a Fourier transform of the image. (B) Higher-magnification SEM image of the sample in (A). (C) Spin-coated monolayer colloidal crystal. (D) Pair correlation function (PCF) calculated from a lower-magnification SEM image of the monolayer sample in (C). For comparison, the PCF for an ideal hexagonal lattice with  $\sqrt{2}D$  center-to-center distance is also shown (black lines).

suggesting a similar shear-induced ordering mechanism for the observed colloidal crystallization process [28]. As revealed by previous shear-induced colloidal crystallization studies, the high shear rate ( $>10^3$ ) in the spin-coating process can lead to a sliding layer mechanism, in which 2D hexagonally packed colloidal layers are readily formed due to the coupling of the centrifugal and viscous forces [36–42]. This shear-alignment process is usually associated with the reduction of the viscosity of the colloidal suspensions (i.e., shear thinning) due to the reduced resistance when layers of ordered spheres glide over one another [36, 42]. Figure 3 shows the comparison of the shear thinning behavior for colloidal suspensions using spheres with diameters of 350 and 70 nm at the same particle volume fraction (0.20). It is apparent that a higher shear rate is required to achieve low relative viscosity for 70 nm particles compared to 350 nm spheres, indicating that a higher spin speed is necessary to crystallize smaller particles. This agrees with our experimental observation that the crystallization of 70 nm particles only occurs at high spin speed ( $\geq 10\,000$  rpm). This result correlates well with early shear-annealing studies [42, 43]. Electrostatic repulsion between silica nanoparticles could contribute to the observed non-close-packed structure as zeta potential measurements show that the nanoparticles are charged ( $\zeta = -44.8 \pm 3.2$  mV) in the silica–ETPTA suspensions.

The current spin-coating technique for assembling sub-100 nm diameter particles over a large area was taken one step further by using the non-close-packed colloidal monolayers as templates to pattern self-cleaning, broadband antireflection coatings directly on crystalline silicon substrates. The silica nanoparticles were used as etching masks during a chlorine

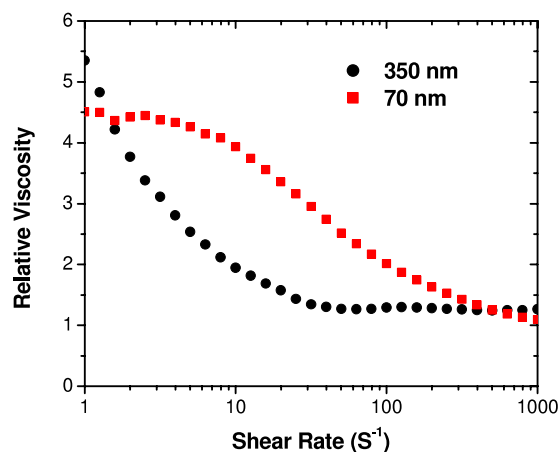


**Figure 3.** Shear thinning behavior of silica–ETPTA suspensions using 70 and 350 nm particles at a volume fraction of 0.2.

RIE process operating at 3 mTorr pressure, 20 SCCM flow rate, and 50 W to generate silicon nanopillars underneath them (see the tilted SEM image in figure 4(A)). Figures 4(B) and (C) show top-view and side-view SEM images of an array of templated nanopillars after dissolving silica nanoparticles in a 2% hydrofluoric acid aqueous solution. The preservation of the hexagonal ordering and the interparticle distance of the templating silica monolayer are apparent for the resulting nanopillar arrays. The depth of the templated nanopillars can be controlled by changing the RIE duration. Figure 4(D) shows a cross-sectional SEM image of an array of silicon nanopillars with aspect ratio of  $\sim 6.0$  after 20 min of Cl<sub>2</sub> RIE. Shallow

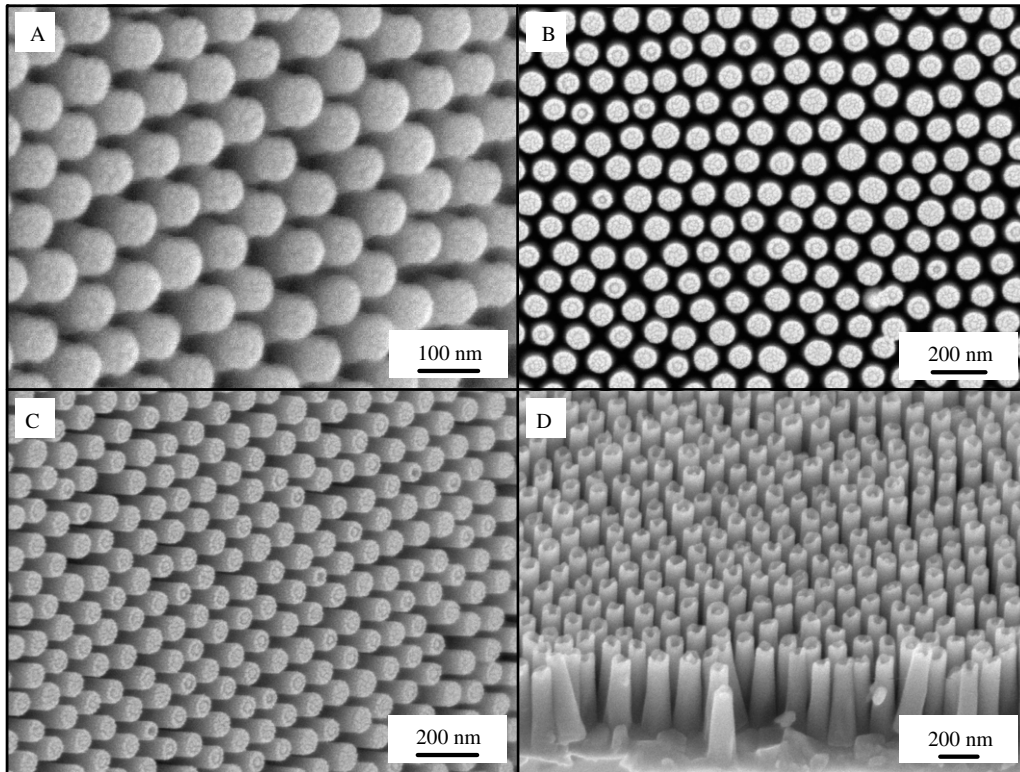


**Figure 4.** (A) Tilted-view ( $20^\circ$ ) SEM image showing the templating silica nanoparticles and the underneath silicon nanopillars after brief  $\text{Cl}_2$  RIE. (B) Top-view SEM image of a templated silicon nanopillar array after 15 min RIE. (C) Tilted-view ( $20^\circ$ ) SEM image of the sample in (B). (D) Cross-sectional SEM image of silicon nanopillars etched for 20 min.

dimples are formed on the top surfaces of the pillars due to the shrinkage of the templating silica nanoparticles during prolonged etching that makes the silica particles too small to protect the silicon underneath from being etched. The number density of the templated nanopillars ( $1.5 \times 10^{10}$  pillars  $\text{cm}^{-2}$ ) is more than one order of magnitude higher than that of the samples templated from submicrometer-scale particles [44].

The templated silicon nanopillar arrays were dark, and no angle-dependent diffraction was observed as the periodicity of the nanopillar arrays is much smaller than the wavelength of visible light. The specular reflection of the templated nanopillar arrays was evaluated using visible–near-infrared reflectivity measurement at normal incidence and theoretical calculation based on a rigorous coupled-wave analysis (RCWA) model [45]. Figure 5 compares the specular reflection from a flat silicon wafer, a commercial crystalline silicon solar cell with vapor-deposited silicon nitride ( $\text{SiN}_x$ ) antireflection coating, and the templated nanopillar array as shown in figure 4(D). The normal-incidence reflection is greatly reduced from  $>30\%$  for a flat silicon wafer to  $<2.5\%$  for the templated nanopillar array. It is also apparent that the nanopillar ARC exhibits excellent broadband antireflection property, better than commercial ARC on the crystalline silicon solar cell, which shows reduced reflection only around 600–800 nm [46].

The experimental reflection measurement was complemented by a theoretical calculation using a rigorous coupled-wave analysis (RCWA) model [45]. We assume that the templated pillars have a shape like inverted circular paraboloid. A

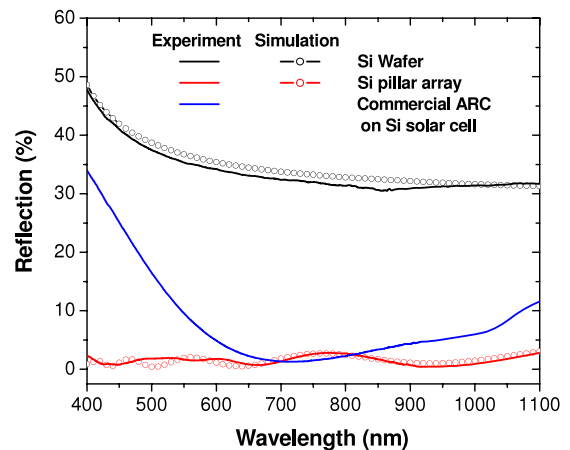


**Figure 5.** Experimental and simulated specular reflection at normal incidence from a flat silicon wafer (black), a commercial single-crystalline silicon solar cell with  $\text{SiN}_x$  antireflection coating (blue), and the templated silicon nanopillar array as shown in figure 4(D) (red).

coordinate system is set up with the  $z$ -axis perpendicular to the pillar surface so that the array troughs are at  $z = 0$  and the pillar peaks at  $z = h$ . We divide the pillar arrays into  $N = 100$  horizontal layers with thickness  $\frac{h}{N}$ . The  $z$ -coordinate  $z^*$  and the radius  $r^*$  of each layer satisfy  $r^* = r\sqrt{1 - \frac{z^*}{h}}$ , where  $0 \leq z^* \leq h$ . The pillar lattice is assumed to be hexag-

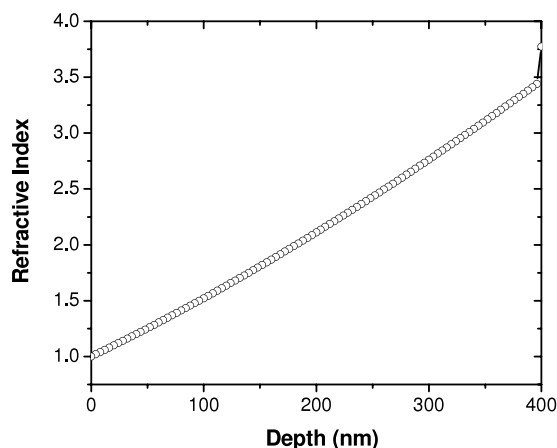


**Figure 6.** Change of the calculated effective refractive index at  $\lambda = 700$  nm from the wafer surface (depth = 0) to the bottom of templated silicon pillars with 400 nm height.

onal and the distance between the centers of the neighboring troughs is defined as  $\sqrt{2}D$  (figure 2(D)). Therefore, the horizontal layer at level  $z^*$  contains a fraction  $f(z^*)$  of silicon with complex refractive index  $\tilde{N}_{\text{Si}} = n + ik$  ( $n$  and  $k$  are the optical constants of silicon) [47], and a fraction  $1 - f(z^*)$  of air with refractive index  $n_{\text{air}} = 1$ . The hexagonal structure of the pillar arrays leads to the formula  $f(z^*) = \frac{\pi(r^*)^2}{\sqrt{3}D^2}$ . Based on the effective medium theory, the effective refractive index  $n(z^*)$  of the layer at height  $z^*$  can be approximated by  $n(z^*) = [f(z^*)\tilde{N}_{\text{Si}}^q + (1 - f(z^*))n_{\text{air}}^q]^{\frac{1}{q}}$ , where  $q = \frac{2}{3}$  [11, 48]. We finally calculate the reflectance of the whole system by solving the Maxwell equation to express the electromagnetic (EM) field in each layer and then matching the EM boundary conditions between neighboring layers for the determination of the reflectance of the system.

Figure 5 shows that the simulated spectra (dotted lines) for both the flat silicon substrate and the templated nanopillar array agree well with the experimental results. The excellent broadband antireflection of the nanopillar ARCs is due to the refractive index gradient across the air and silicon interface [11]. Figure 6 shows the calculated effective refractive index at  $\lambda = 700$  nm across the height of 400 nm nanopillars. For the bare wafer, the refractive index (RI) changes sharply from air (RI = 1.0) to bulk silicon (RI = 3.774), while for templated nanopillars, the RI changes gradually from 1.0 to 3.439 and then to 3.774. This refractive index gradient leads to very low reflection over a wide range of wavelengths.

The templated nanopillars with high aspect ratio can trap a high fraction of air in the trough area between nanopillars, making the silicon surface superhydrophobic [49]. This is promising for developing self-cleaning ARCs for silicon solar cells. The hydrophobicity of silicon nanopillars can be further improved by functionalization with fluorosilane through the well-established silane coupling reaction [50]. Here, silicon nanopillars were chemically modified by reacting with a  $4.4 \times 10^{-3}$  M solution of (heptadecafluoro-1,1,2,2-tetrahydrodecyl)trichlorosilane (Gelest) in hexane/ $\text{CCl}_4$

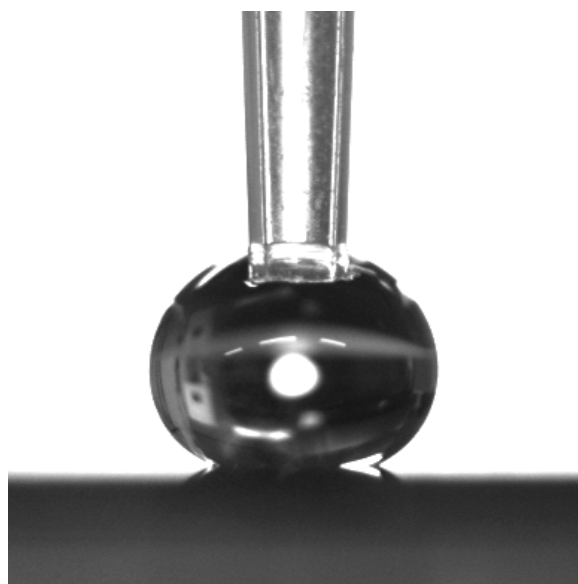


**Figure 7.** Water drop profile on a fluorosilane-modified silicon nanopillar array prepared by  $\text{Cl}_2$  RIE for 20 min using 70 nm silica nanoparticles as templates.

(v/v:70/30) for 2 h at room temperature. The resulting surfaces were rinsed with dichloromethane and ethanol and then dried under air. Figure 7 shows a water drop profile on a fluorosilane-modified silicon nanopillar array. The surface is superhydrophobic and the measured apparent water contact angle is  $158^\circ$ , significantly enhanced from  $\sim 108^\circ$  on a fluorinated flat silicon wafer. The utilization of nanoparticles instead of submicrometer-sized particles as templates to generate moth-eye ARCs facilitates the elimination of unwanted Bragg diffraction and simultaneously enhances the film hydrophobicity [11, 49].

#### 4. Conclusions

In conclusion, we have developed a simple and scalable templating approach for fabricating sub-100 nm periodic nanostructures with resolution beyond the optical diffraction limit. Non-close-packed colloidal crystals consisting of 70 nm silica nanoparticles can be rapidly assembled over large area by a simple spin-coating technique. The shear-aligned colloidal monolayers can be used as structural templates to pattern subwavelength moth-eye ARCs directly on silicon substrates. The templated nanopillar arrays exhibit excellent broadband antireflection and superhydrophobic properties, which are promising for developing self-cleaning ARCs for crystalline silicon solar cells.

#### Acknowledgments

This work was supported in part by the NSF under Grant Nos CBET-0651780 and CBET-0744879, ACS Petroleum Research Fund, and the UF Research Opportunity Incentive Seed Fund.

**References**

- [1] Sun S H, Murray C B, Weller D, Folks L and Moser A 2000 *Science* **287** 1989–92
- [2] Pham H H, Gourevich I, Oh J K, Jonkman J E N and Kumacheva E 2004 *Adv. Mater.* **16** 516–20
- [3] Levene M J, Korlach J, Turner S W, Foquet M, Craighead H G and Webb W W 2003 *Science* **299** 682–6
- [4] Xu M, Goponenko A V and Asher S A 2008 *J. Am. Chem. Soc.* **130** 3113–9
- [5] Zheng S P, Ross E, Legg M A and Wirth M J 2006 *J. Am. Chem. Soc.* **128** 9016–7
- [6] Kuo C W, Shiu J Y, Wei K H and Chen P 2007 *J. Chromatogr. A* **1162** 175–9
- [7] Shevchenko E V, Talapin D V, Kotov N A, O'Brien S and Murray C B 2006 *Nature* **439** 55–9
- [8] Veinot J G C, Yan H, Smith S M, Cui J, Huang Q L and Marks T J 2002 *Nano Lett.* **2** 333–5
- [9] Lohmuller T, Helgert M, Sundermann M, Brunner R and Spatz J P 2008 *Nano Lett.* **8** 1429–33
- [10] Huang Y F *et al* 2007 *Nat. Nanotechnol.* **2** 770–4
- [11] Stavenga D G, Foletti S, Palasantzas G and Arikawa K 2006 *Proc. R. Soc. B* **273** 661–7
- [12] Chattopadhyay S, Chen L C and Chen K H 2006 *Crit. Rev. Solid State Mater. Sci.* **31** 15–53
- [13] Clapham P B and Hutley M C 1973 *Nature* **244** 281–2
- [14] Gombert A, Glaubitt W, Rose K, Dreiholz J, Blasi B, Heinzel A, Sporn D, Doll W and Wittwer V 1999 *Thin Solid Films* **351** 73–8
- [15] Huang J Y, Wang X D and Wang Z L 2008 *Nanotechnology* **19** 025602
- [16] Choi D G, Yu H K, Jang S G and Yang S M 2004 *J. Am. Chem. Soc.* **126** 7019–25
- [17] Haynes C L and Van Duyne R P 2001 *J. Phys. Chem. B* **105** 5599–611
- [18] Hulteen J C and Van Duyne R P 1995 *J. Vac. Sci. Technol. A* **13** 1553–8
- [19] Kosiorek A, Kandulski W, Chudzinski P, Kempa K and Giersig M 2004 *Nano Lett.* **4** 1359–63
- [20] Zhang G and Wang D Y 2008 *J. Am. Chem. Soc.* **130** 5616–7
- [21] Zhang G, Wang D Y and Mohwald H 2007 *Nano Lett.* **7** 127–32
- [22] Haes A J, Hall W P, Chang L, Klein W L and Van Duyne R P 2004 *Nano Lett.* **4** 1029–34
- [23] Rybczynski J, Ebels U and Giersig M 2003 *Colloids Surf. A* **219** 1–6
- [24] Jang S G, Yu H K, Choi D G and Yang S M 2006 *Chem. Mater.* **18** 6103–5
- [25] Stewart M E, Anderton C R, Thompson L B, Maria J, Gray S K, Rogers J A and Nuzzo R G 2008 *Chem. Rev.* **108** 494–521
- [26] Wong S, Kitaev V and Ozin G A 2003 *J. Am. Chem. Soc.* **125** 15589–98
- [27] Vlasov Y A, Bo X Z, Sturm J C and Norris D J 2001 *Nature* **414** 289–93
- [28] Jiang P and McFarland M J 2004 *J. Am. Chem. Soc.* **126** 13778–86
- [29] Jiang P, Prasad T, McFarland M J and Colvin V L 2006 *Appl. Phys. Lett.* **89** 011908
- [30] Jiang P and McFarland M J 2005 *J. Am. Chem. Soc.* **127** 3710–1
- [31] Jiang P 2006 *Langmuir* **22** 3955–8
- [32] Sun C H, Min W L and Jiang P 2008 *Chem. Commun.* 3163–5
- [33] Henzie J, Lee M H and Odom T W 2007 *Nat. Nanotechnol.* **2** 549–54
- [34] Johnson S A, Ollivier P J and Mallouk T E 1999 *Science* **283** 963–5
- [35] Arriagada F J and Osseo-Asare K 1999 *J. Colloid Interface Sci.* **211** 210–20
- [36] Ackerson B J 1990 *J. Phys.: Condens. Matter* **2** SA389–92
- [37] Ackerson B J and Pusey P N 1988 *Phys. Rev. Lett.* **61** 1033–6
- [38] Amos R M, Shepherd T J, Rarity J G and Tapster P 2000 *Electron. Lett.* **36** 1411–2
- [39] Chen L B, Ackerson B J and Zukoski C F 1994 *J. Rheol.* **38** 193–216
- [40] Hoffman R L 1972 *Trans. Soc. Rheol.* **16** 155–65
- [41] Pieranski P 1983 *Contemp. Phys.* **24** 25–73
- [42] Vermant J and Solomon M J 2005 *J. Phys.: Condens. Matter* **17** R187–216
- [43] Lee J D, So J H and Yang S M 1999 *J. Rheol.* **43** 1117–40
- [44] Sun C H, Jiang P and Jiang B 2008 *Appl. Phys. Lett.* **92** 061112
- [45] Moharam M G, Pommet D A, Grann E B and Gaylord T K 1995 *J. Opt. Soc. Am. A* **12** 1077–86
- [46] Doshi P, Jellison G E and Rohatgi A 1997 *Appl. Opt.* **36** 7826–37
- [47] Palik E D (ed) 1991 *Handbook of Optical Constants of Solids* (Boston: Academic)
- [48] Macleod H A 2001 *Thin-Film Optical Filters* (Bristol: Institute of Physics Publishing)
- [49] Sun T L, Feng L, Gao X F and Jiang L 2005 *Acc. Chem. Res.* **38** 644–52
- [50] Coffinier Y, Janel S, Addad A, Blossey R, Gengembre L, Payen E and Boukherroub R 2007 *Langmuir* **23** 1608–11